Computer Modeling in Engineering & Sciences

Tech Science Press

https://doi.org/10.32604/cmes.2026.086381

ARTICLE

# Aerodynamic Performances of a Parked Ten-Megawatt Class Wind Turbine in the Extreme Typhoon Conditions

**Congbo Zheng[1], Qian Chen[2], Zeshuai Chen[2], Tianyu Song[1], Ruiliang Wang[2,*], Chaojin Chen[1], Dongliang Yu[1] and Di Tang[1]**

[1]College of Mechanical Engineering, Zhejiang University of Technology, Hangzhou, China
[2]Zhejiang Key Laboratory of Offshore Wind Power Technology, Windey Energy Technology Group Co., Ltd., Hangzhou, China
*Corresponding Author: Ruiliang Wang. Email: wangrl@windeyenergy.com

Received: 29 May 2026; Accepted: 26 August 2026; Published: 21 October 2026

**ABSTRACT:** Ultra-large wind turbines in typhoon-prone regions remain exposed to complex unsteady aerodynamic loads even after entering the parked state, which may induce severe structural damage or even structural failure under extreme typhoon conditions. This study numerically investigates the directional aerodynamic response of a 10-MW class parked wind turbine with a rotor diameter of 220 m and a tower height of 130 m. Furthermore, the computer modeling employs a two-stage numerical procedure in conjunction with eight representative directional inflow cases defined with reference to recent severe-typhoon observations, thereby enabling a systematic assessment of the mean aerodynamic loads, load fluctuations, dominant frequencies, surface-pressure distributions, separated-flow structures, and blade–tower wake interactions of the ultra-large wind turbine under typhoon wind conditions. The simulations reveal pronounced directional asymmetry in the parked-turbine aerodynamic performances, with distinct differences between mean-load-dominated and fluctuation-dominated extreme conditions. Further analysis shows that directional load redistribution is governed by the combined effects of surface-pressure concentration, blade-flow separation, tower-wake development, and aerodynamic interactions among the blades, nacelle, and tower. These findings improve the understanding of the directional aerodynamic behavior of ultra-large parked wind turbines under extreme typhoon conditions and provide useful support for aerodynamic-load assessment and parked-state safety evaluation.

**KEYWORDS:** Ultra-large wind turbine; computer modeling; parked state; aerodynamic performances; extreme typhoon conditions

## 1 Introduction

Against the background of the global low-carbon energy transition, wind energy has become an important tower for optimizing energy structures. According to the Global Wind Report 2026 published by the Global Wind Energy Council, which reports global wind-power statistics for 2025, 165 GW of new wind power capacity was installed worldwide in 2025, bringing the cumulative global installed wind capacity to 1299 GW [1]. China, in particular, had a cumulative installed wind power capacity of 640.626 GW by the end of 2025, including 47.390 GW of offshore wind power [2]. With the development of offshore wind power toward deeper waters and larger unit capacities, the rated capacity, blade length, hub height, and rotor swept area of wind turbines have continued to increase. The selection of rotor size is also closely related to site-specific wind-resource characteristics. For relatively low-wind-speed sites, including some areas in eastern China where near-surface wind speeds have shown a sustained weakening trend, enlarging the rotor swept

Copyright © 2026 The Authors. Published by Tech Science Press. This work is licensed under a Creative Commons Attribution 4.0 International License, which permits unrestricted use, distribution, and reproduction in any medium, provided the original work is properly cited.

area can improve energy capture and power production over the more frequently occurring sub-rated wind-speed range [3,4]. Previous studies have further shown that increasing the rotor swept area without increasing the rated power can effectively enhance power capture under low-wind-speed conditions, providing a practical basis for low-specific-rating rotor designs [5]. However, many wind-energy development areas along the eastern and southeastern coasts of China are also exposed to severe typhoon conditions. Increasing the rotor swept area also expands the spatial extent over which the turbine is exposed to highly non-uniform typhoon inflow, making the associated unsteady aerodynamic responses to wind-speed variations, abrupt wind-direction changes, and high turbulence an important concern for ultra-large wind turbines.

Typhoon activity is frequent along the southeastern coast and offshore regions of China, where coastal and offshore wind farms are persistently exposed to extreme wind conditions. According to the Chinese national standard for tropical cyclone intensity classification, GB/T 19201—2006 [6], a tropical cyclone is classified as a typhoon when the maximum sustained wind speed near its center reaches 32.7 m/s and above. The wind speeds of severe typhoons and super typhoons can reach 41.5–50.9 m/s and 51.0 m/s and above, respectively, which are significantly higher than the cut-out wind speed of wind turbines during normal operation. In general, wind turbines can still generate a certain amount of power under low and medium-intensity tropical cyclones, such as tropical depressions and tropical storms. However, when the wind speed reaches the level of a severe tropical storm or above, the turbine usually enters protective states such as shutdown, feathering, braking, or yaw locking [7]. As summarized in Table 1, statistics of tropical cyclones making landfall in China from 2017 to 2025 show that a total of 107 tropical cyclones made landfall during the nine-year period, of which 31 were classified as destructive tropical cyclones, accounting for 28.97%. This indicates that wind turbines in typhoon-prone regions face a high risk of extreme wind loading. Although IEC 61400-1 specifies the fundamental requirements for wind turbine structural integrity design [8], the prescribed extreme wind conditions may still be insufficient to provide adequate safety margins in some typhoon-affected regions [9]. Meanwhile, under the influence of climate change, offshore extreme wind speeds are generally increasing worldwide, and some existing and planned offshore wind farms may face the risk of wind speeds exceeding the design thresholds of corresponding turbine classes [10]. For ultra-large wind turbines, whose blade length and tower height reach the hundred-meter scale, the rotor swept area covers a much larger spatial range. As a result, wind-speed gradients, turbulence-intensity variations, and rapid wind-direction shifts within the typhoon boundary layer can produce pronounced spatially non-uniform inflow at the whole turbine scale.

Previous accident investigations have shown that, under severe typhoons or super typhoons, wind turbines may still suffer blade fracture, tower buckling, connection failure, or even complete structural collapse, even when they are in a parked protective state. In 2006, Super Typhoon Saomai made landfall in Cangnan, Zhejiang Province, China, causing varying degrees of damage to 27 wind turbines at the Heding Mountain wind farm. Among them, five towers collapsed and 33 blades were damaged, resulting in direct economic losses of approximately 70 million RMB. Based on meteorological tower measurements, Li et al. [11] indicated that the accident was closely related to abnormally strong winds, intense turbulence, and rapid wind-direction changes. In 2010, Typhoon Megi affected the coastal region of Fujian Province and caused damage to several wind turbines [12]. In 2015, Severe Typhoon Soudelor struck a wind farm near Taichung Harbor in Taiwan, where the nacelle SCADA system recorded a maximum instantaneous wind speed exceeding 59.5 m/s, leading to the collapse of several 2.0 MW wind turbine towers [13,14]. These accidents demonstrate that typhoon-induced structural failure is not caused by mean wind speed alone, but rather by the combined effects of extreme wind speed, strong turbulence, abrupt wind-direction changes, yaw misalignment, and parked rotor posture.

**Table 1:** Classification of tropical cyclone and investigation on typhoon landing China from 2017 to 2025.

| Year | Landing Times | Economic | | Defensive | | Destructive | | Super Typhoon | |
|---|---|---|---|---|---|---|---|---|---|
| | | Landing | Percent | Landing | Percent | Landing | Percent | Landing | Percent |
| 2017 | 11 | 5 | 45.45% | 3 | 27.27% | 3 | 27.27% | 0 | 0.00% |
| 2018 | 20 | 16 | 80.00% | 2 | 10.00% | 2 | 10.00% | 0 | 0.00% |
| 2019 | 11 | 8 | 72.73% | 1 | 9.09% | 2 | 18.18% | 1 | 9.09% |
| 2020 | 6 | 2 | 33.33% | 1 | 16.67% | 3 | 50.00% | 0 | 0.00% |
| 2021 | 10 | 6 | 60.00% | 2 | 20.00% | 2 | 20.00% | 0 | 0.00% |
| 2022 | 8 | 4 | 50.00% | 1 | 12.50% | 3 | 37.50% | 0 | 0.00% |
| 2023 | 12 | 5 | 41.67% | 2 | 16.67% | 5 | 41.67% | 0 | 0.00% |
| 2024 | 9 | 2 | 22.22% | 1 | 11.11% | 6 | 66.67% | 0 | 0.00% |
| 2025 | 20 | 8 | 40.00% | 7 | 35.00% | 5 | 25.00% | 0 | 0.00% |
| 2017~2025 | 107 | 56 | 52.34% | 20 | 18.69% | 31 | 28.97% | 1 | 0.93% |

Note: Economic, Defensive, and Destructive represent mutually exclusive impact categories, and their counts sum to the total number of landfalling tropical cyclones. The Super typhoon column is an additional intensity-based statistic that may overlap with these categories and is therefore not included in their sum.

Typhoon wind fields are characterized by pronounced non-stationarity, spatial non-uniformity, and directional uncertainty. Tang et al. [7] developed a typhoon wind-field model based on observational data, incorporating different wind speeds, wind directions, and turbulence intensities. Their results showed that these factors significantly alter the surface pressure distribution and aerodynamic load response of parked blades. Compared with conventional atmospheric boundary-layer inflow, the wind speed during typhoon passage often exhibits a multi-stage evolution, including rapid intensification, short-term weakening, and subsequent re-intensification. When the eyewall approaches, a wind turbine may simultaneously experience high mean wind speed, strong gusts, and severe wind-direction shifts within a short period. Recent typhoons over the western North Pacific and South China Sea provide representative examples of such high-wind conditions. For example, in 2024, Super Typhoons Gaemi and Yagi reached maximum sustained wind speeds of 58 and 68 m/s, respectively. Yagi also underwent rapid intensification over the South China Sea before making landfall near Wenchang, Hainan Province, with a maximum wind speed of 62 m/s [15]. In 2025, Super Typhoon Ragasa reached a lifetime maximum intensity of 62 m/s [16]. These observations indicate that sustained wind speeds in recent intense typhoons over the western North Pacific and South China Sea can approach 70 m/s. For ultra-large wind turbines, because both blade length and tower height reach the hundred-meter scale, the larger rotor swept area makes wind-speed gradients, turbulence-intensity variations, and wind-direction shifts within the typhoon boundary layer more likely to generate distinct non-uniform inflow along the blade span and across the entire turbine.

In addition to variations in mean wind speed and wind direction, typhoon turbulence characteristics also have a significant influence on the unsteady loads of parked wind turbines. Masters et al. [17] analyzed near-surface wind-speed observations in tropical cyclones and pointed out that turbulence intensity, gust factor, peak factor, and integral length scale in tropical cyclones exhibit substantial scatter. Therefore, the direct use of conventional wind-field assumptions may be insufficient for accurately describing transient aerodynamic responses under typhoon conditions. Typhoons are often accompanied by heavy rainfall; however, existing structural failure simulations have shown that the contribution of rainfall to the total wind turbine load is relatively limited and can be approximately neglected in analyses dominated by aerodynamic loading [13]. In addition, based on meteorological tower data from the coastal region of South China,

Song et al. [18] reported that actual wind profiles in the typhoon boundary layer may deviate significantly from conventional power-law distributions when the observation site is close to the typhoon center or eyewall. Yi et al. [19] further demonstrated that although the mean wind-speed profile and turbulence-intensity profile under typhoon conditions can be approximately described by power laws, their exponents are generally higher than the values specified in design standards and vary with typhoon intensity and the relative position of the observation site. For ultra-large wind turbines, such uncertainties in wind-speed and turbulence profiles can cause different blade-span locations to experience different inflow conditions, thereby intensifying pressure fluctuations on the blade, nacelle, and tower surfaces, as well as load imbalance at the turbine scale.

Under typhoon action, wind turbine structural failures commonly manifest as blade damage, tower collapse, and connection failure [20]. For blades, strong gusts and periodic unsteady loads may induce local laminate damage, leading- and trailing-edge cracking, crack propagation in the blade-root connection region, and even complete blade fracture [21,22]. For towers, extreme bending moments, fluctuating wind pressure, yaw misalignment, and coupled tensile-shear effects in connecting bolts may lead to local tower buckling, bolt fracture, and overall instability [23]. Meanwhile, welded joints are also critical weak points under strong winds and cyclic aerodynamic loading. Weld geometry, welding quality, and local notch effects can significantly affect the fatigue performance of wind turbine towers [24]. As wind turbines continue to evolve toward ultra-large scales, blade size, tower height, and structural flexibility further increase, and typhoon-induced low-frequency unsteady loads and aerodynamic interactions among components may become more prominent. Therefore, before conducting structural safety assessment, it is necessary to first clarify the surface pressure distribution, load fluctuation characteristics, and flow-field evolution of ultra-large parked wind turbines under typhoon conditions.

In terms of numerical simulation, engineering tools such as FAST/OpenFAST and AeroDyn have been widely used for aeroelastic response analysis and aerodynamic load prediction of wind turbines [25,26]. These methods can account for aerodynamic forces, structural elasticity, and turbulent inflow, and are suitable for engineering assessments of ultimate and fatigue loads. However, their aerodynamic models are generally based on blade element momentum theory, dynamic wake models, or engineering correction methods. Although they are computationally efficient for both operating and parked-state engineering analyses, their ability to resolve high-angle-of-attack blade flow, flow separation, component shielding, and local vortex structures under parked conditions is limited. By contrast, computational fluid dynamics can directly solve the three-dimensional flow field around wind turbines and provide unsteady pressure distributions on the blade, nacelle, and tower surfaces. The two-equation eddy-viscosity turbulence model proposed by Menter [27] provides an important basis for predicting boundary-layer separation in engineering flow problems. Sørensen et al. [28] conducted numerical predictions of the NREL Phase VI rotor by solving the Navier–Stokes equations and verified the applicability of CFD methods to wind turbine aerodynamic analysis. Different CFD approaches exhibit different levels of applicability under typhoon conditions. RANS methods have relatively high computational efficiency and are suitable for engineering-scale parametric analyses, but under conditions involving strong separation, high turbulence, and pronounced large-scale vortex shedding, they may damp transient vortex structures and affect the accuracy of unsteady load-fluctuation prediction. LES and DES methods are better suited for capturing large-scale unsteady vortex structures. The subgrid-scale model proposed by Smagorinsky [29] laid the foundation for LES, while the hybrid RANS/LES approach proposed by Spalart et al. [30] promoted the application of DES to high-Reynolds-number complex flows. Nevertheless, for full-scale ultra-large wind turbines, LES and DES impose high requirements on grid resolution, near-wall treatment, and computational resources, which still limits their engineering application in multi-directional and multi-condition typhoon simulations. Therefore,

achieving a balance between computational efficiency and the ability to resolve unsteady flow structures remains a key issue in the simulation of aerodynamic loads on ultra-large wind turbines under typhoon conditions. Polar-based BEM or dynamic-wake methods can provide efficient estimates of integrated aerodynamic loads, but they cannot directly resolve the pressure redistribution, component shielding and separated vortex structures around a fully feathered parked rotor. DES or LES would be expected to provide richer tower-wake shedding spectra than URANS, although their computational cost remains prohibitive for the present full-scale, eight-direction whole-turbine simulations.

In summary, existing studies have extensively addressed the typhoon resistance of wind turbines from the perspectives of typhoon-induced accident investigations, typhoon wind-field characteristics, structural failure mechanisms, and numerical simulation methods. However, the aerodynamic interaction mechanisms among the blades, nacelle, and tower of ultra-large parked wind turbines with hundred-meter-scale blades and towers remain insufficiently investigated. In this study, an ultra-large parked horizontal-axis wind turbine located in a typhoon-prone region is selected as the research object. Based on actual meteorological records, a simplified directional extreme-wind inflow model characterized by high mean wind speed and multiple fixed inflow directions is established, and three-dimensional unsteady CFD simulations are conducted to investigate the extreme aerodynamic load characteristics of the hundred-meter-scale blades, high tower, and full turbine system. First, the unsteady aerodynamic responses of the isolated tower and rotor are analyzed to reveal the pressure distribution, lift and drag fluctuations, and spectral characteristics at the scale of ultra-large turbine components. Subsequently, a full turbine model consisting of blades, nacelle, and tower is developed to investigate the load variation mechanisms among different components, compare the differences in overall aerodynamic loads under different typhoon inflow directions, and identify critical loading postures of the ultra-large wind turbine in the parked state. The results are expected to provide references for shutdown strategy optimization, extreme wind-load assessment, and typhoon-resistant design of ultra-large wind turbines in typhoon-prone regions.

## 2 Wind Turbine Model

To investigate the unsteady aerodynamic load characteristics of an ultra-large parked wind turbine under extreme typhoon conditions, a horizontal-axis wind turbine with hundred-meter-scale blades is selected as the research object, and a three-dimensional numerical model is established. The turbine adopts an upwind configuration and is characterized by variable-pitch and variable-speed operation.

### *2.1 Models of Tower, Rotor and the Turbine*

As shown in Fig. 1a, the wind turbine model consists of a tower, nacelle, rotor, and blades. This study focuses on the unsteady aerodynamic characteristics of the blades and tower. To simplify the modeling procedure while retaining the principal geometric features, a conventional tubular tower fixed at the ground is adopted to represent a large-scale wind turbine. The tower is modeled as a tapered cylindrical structure with a total height of 130 m, a bottom diameter of 15.0 m, and a top diameter of 9.76 m. The nacelle is simplified as a cylindrical body with a diameter of 9.2 m and a length of 14 m, respectively. The rotor hub is simplified as a conical body with a diameter of 7.35 m, a cone angle of −6°, and a tilt angle of 7°, as shown in Fig. 1b. The vertical offset and overhang distance are 3.1 and 5.3 m, respectively. The blade length is 110.0 m, and the blade offset is set to 0. The cut-in and cut-out wind speeds of the turbine are 3 and 25 m/s, respectively. Under operating conditions, the pitch angle is set to 0° to achieve maximum wind-energy utilization, whereas under parked conditions, it is set to 90° to enhance wind-resistance stability. Fig. 1c shows the top and side views of the rotor configuration under parked conditions.

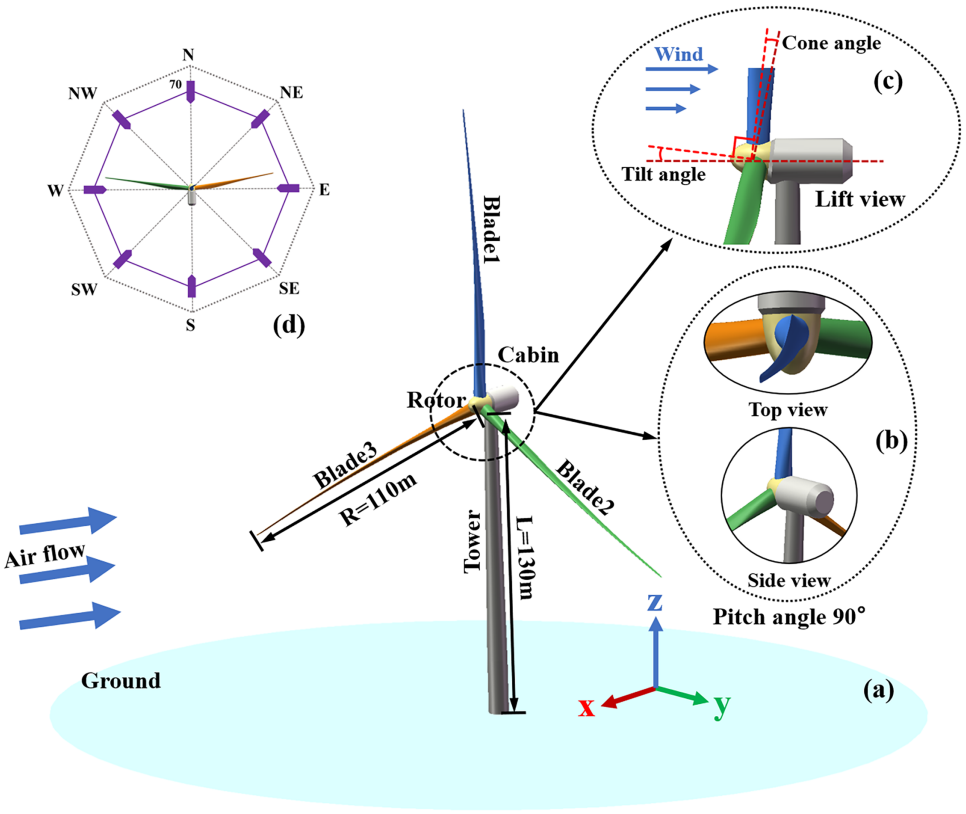



**Figure 1:** Wind turbine model in the current study: (**a**) parked wind turbine; (**b**) local view of the rotor in the parked state; (**c**) schematic diagram of the left side of the inclination and cone angles; (**d**) schematic of the wind model.

When a wind turbine is subjected to extreme wind conditions such as typhoons, it generally enters a parked protection state, in which the blades are feathered, the rotor is braked, and the yaw system may be locked or operated with limited adjustment capability. Previous studies have shown that the aerodynamic loads on a parked wind turbine are closely related to the blade azimuth angle, yaw angle, and the orientation of the blades relative to the incoming flow. In particular, under strong wind conditions, different parked rotor positions can alter the shielding relationship and wake interference among the blades, nacelle, and tower, thereby causing substantial differences in the extreme loads acting on the blades and tower. Nelson et al. found in their study of extreme typhoon loads that the rotor thrust reaches a relatively high level when a single blade is positioned vertically upward [31]. Therefore, to account for a relatively critical loading condition, the parked position in which the upper blade is aligned with the tower axis is selected as the initial rotor posture for the subsequent numerical simulations. In the present simulations, all three blades were fully feathered with a pitch angle of 90°, and the braked rotor was kept at a fixed azimuth for all inflow directions. This fixed-azimuth arrangement provides a deterministic reference state for comparing directional aerodynamic-load redistribution, while the influence of free idling and other parked azimuth positions is left for future work.

### *2.2 Typhoon Character and Wind Estimate*

The incoming wind field under typhoon conditions is characterized by pronounced non-stationarity and directional uncertainty. The wind speed generally increases gradually to a peak as the outer circulation of the typhoon approaches the eyewall region. When the typhoon eye passes near the observation site, the local wind speed decreases temporarily; subsequently, as the opposite eyewall approaches, the wind speed

increases rapidly again, forming a double-peak or multi-stage loading process [32]. Such rapidly varying wind-speed histories can subject a parked wind turbine to strong unsteady aerodynamic loads within a short period. For ultra-large wind turbines, the large rotor swept area means that different spanwise locations of the blades may simultaneously experience different local wind speeds and turbulence conditions. Therefore, the wind-speed evolution and spatial non-uniformity of typhoon inflow have a more pronounced influence on their aerodynamic loads.

In addition to extreme mean wind speeds, existing field-measurement-based comparative studies have shown that the turbulence intensity, gust factor, and integral length scale of typhoon wind fields exhibit pronounced scatter and are strongly influenced by surface roughness, measurement height, and the relative position of the observation site with respect to the typhoon center [33]. For ultra-large wind turbines, the coupled effects of high wind speed and strong turbulence can intensify pressure fluctuations on the blade and tower surfaces, thereby increasing the risks of fatigue damage and transient extreme loading. Moreover, rapid wind-direction shifts induced by typhoon circulation may weaken the real-time yaw-tracking capability of the yaw system, forcing the turbine to withstand inflow from different directions under yaw-misaligned or yaw-locked conditions. Considering that different inflow directions can alter the shielding relationship and wake interference among the blades, nacelle, and tower, a representative typhoon wind speed with a typical value of 70 m/s is specified in this study. Eight typical inflow directions are considered, namely N/0°, NE/45°, E/90°, SE/135°, S/180°, SW/225°, W/270°, and NW/315°. These directions are uniformly distributed at equal angular intervals to cover potentially critical loading scenarios that may occur under parked conditions, as illustrated in Fig. 1d. Accordingly, the present inflow model is not intended to reproduce all transient features of a real typhoon boundary layer. Instead, 70 m/s is adopted as a representative severe-typhoon mean inflow speed, because the wind-speed level is consistent with recent severe-typhoon observations over the western North Pacific and South China Sea, where Super Typhoons Gaemi and Yagi reached maximum sustained wind speeds of 58 and 68 m/s, respectively, in 2024 [15], while Super Typhoon Ragasa reached a lifetime maximum intensity of 62 m/s in 2025 [16]. In the present simulations, turbulence fluctuations, wind shear, and wind veer are simplified to focus on the effect of inflow direction. Accordingly, the eight fixed inflow directions are used as representative directional extreme-wind cases, rather than as a full reconstruction of the typhoon boundary layer, to examine the load redistribution among the blades, nacelle, and tower under the same mean wind speed.

## 3 Numerical Methods

### *3.1 CFD Method*

In the parked condition, the airflow around the wind turbine is governed by the incompressible unsteady Navier–Stokes equations. Since the rotor is locked and the turbine is in a stationary state, no rotating reference frame is required to describe rotor motion. The present numerical simulations focus on the unsteady external flow surrounding the fixed three-dimensional geometry of the wind turbine. The governing equations for incompressible unsteady flow are expressed as:

$$\frac{\partial \mathbf{u}}{\partial t} + \mathbf{u} \cdot \nabla \mathbf{u} = -\frac{1}{\rho} \nabla p + \nu \nabla^2 \mathbf{u} + \nabla \cdot \left( \nu_t \nabla \mathbf{u} \right) \tag{1}$$

$$\nabla \cdot \mathbf{u} = 0 \tag{2}$$

where $\mathbf{u}$ is the velocity vector, $p$ is the pressure, $\rho$ is the air density, $\nu$ is the kinematic viscosity, and $\nu_t$ is the turbulent eddy viscosity.

To accurately capture transition phenomena and the associated flow structures around the turbine, the γ–Re($\theta_t$) Transition SST model was adopted, which is based on the SST k-omega formulation and additionally introduces transport equations related to intermittency γ and the transition momentum-thickness Reynolds number Re(θt). The model retains the well-established capability of SST in predicting adverse-pressure-gradient and wall-separated flows, while providing a more detailed description of local near-wall boundary-layer development. Although the flow under the present 70 m/s inflow condition is largely turbulent at the full-turbine scale, the parked feathered configuration may still produce complex local flow features, such as low-speed recirculation, incipient separation and tower–nacelle interference around the blade, nacelle and tower surfaces. Therefore, this model was selected to balance the prediction of separated-flow structures and local boundary-layer behavior under extreme wind conditions [7,27]. In the γ–Reθt formulation, the transition model is coupled with the SST turbulence model through the effective intermittency, which modifies the production and destruction terms of the turbulent kinetic-energy equation. The transport equations for turbulent kinetic energy $k$ and specific dissipation rate $\omega$ are expressed as:

$$\frac{\partial k}{\partial t} + \mathbf{u} \cdot \nabla k = \gamma_{eff} P_k - \min\left[\max\left(\gamma_{eff}, 0.1\right), 1.0\right] \beta^* k\omega + \nabla \cdot \left[\left(\nu + \sigma_k \nu_t\right) \nabla k\right] \tag{3}$$

$$\frac{\partial \omega}{\partial t} + \mathbf{u} \cdot \nabla \omega = \alpha^* \frac{\omega}{k} P_k - \beta \omega^2 + \nabla \cdot \left[\left(\nu + \sigma_\omega \nu_t\right) \nabla \omega\right] + 2\left(1 - F_1\right) \frac{\sigma_{\omega 2}}{\omega} \nabla k \cdot \nabla \omega \tag{4}$$

Here, $P_k$ denotes the production term of turbulent kinetic energy, $\gamma_{eff}$ denotes the effective intermittency used for coupling the transition model with the SST formulation, and $F_1$ denotes the SST blending function. The molecular kinematic viscosity and turbulent kinematic viscosity are denoted by $\nu$ and $\nu_t$, respectively, while $\sigma_k$ and $\sigma_\omega$ are the corresponding diffusion coefficients, and $\sigma_{\omega 2}$ is associated with the cross-diffusion term. Correction coefficients are set as $\alpha^* = 1.0$ and $\beta^* = 0.15$ to properly suppress near-wall turbulent viscosity and enhance the accuracy of boundary layer development and vortex shedding predictions around the stationary turbine components, ensuring reliable transition modeling for large-scale wind turbine simulations [7].

A pressure-based transient solver was employed. Pressure–velocity coupling was considered, with second-order discretization for pressure and high-order upwind schemes for momentum. He Green–Gauss cell-based method was used for gradient calculation, and a first-order scheme was used for the turbulence equations. The simulations accurately capture the transient fluid behavior and vortex shedding around the stationary blades and the 130 m tower across eight wind directions, reflecting the coupled blade-tower interactions and directional sensitivity.

A two-stage numerical procedure was adopted for each inflow direction. First, a steady Reynolds-averaged Navier–Stokes (RANS) calculation was performed to establish a converged flow field and obtain the steady aerodynamic loads of the parked turbine. The converged steady-state solution was then used as the initial flow field for the subsequent unsteady Reynolds-averaged Navier–Stokes (URANS) calculation. After the initial transient response had decayed, the aerodynamic-force time histories were recorded and used to determine the load-fluctuation amplitudes and dominant frequencies. Within this framework, the steady RANS solutions were used to characterize the directional aerodynamic-load distributions, while the subsequent URANS simulations were employed to resolve the time-dependent aerodynamic responses and associated load fluctuations. It should be noted that detached-eddy simulation (DES) or large-eddy simulation (LES) could provide a more detailed resolution of broadband tower-wake turbulence, vortex breakdown, and small-scale unsteady flow structures. However, for the present full-scale wind turbine with a rotor diameter of 220 m and a kilometer-scale computational domain, these approaches would

require substantially finer near-wall and wake-region meshes and consequently much higher computational costs. Therefore, the present RANS–URANS framework was adopted as a practical compromise between the resolution of whole-turbine aerodynamic characteristics and the computational requirements of the multi-directional extreme-wind simulations.

### *3.2 Numerical Validation Using a Scaled NH1500 Wind Turbine Test*

To further assess the reliability of the CFD approach for wind turbine aerodynamic prediction, a validation study was conducted using the NH1500 wind turbine benchmark. The experimental data were obtained from the aerodynamic performance test of a 1/16-scale NH1500 wind turbine model carried out on the wind turbine test platform of the China Aerodynamics Research and Development Center (CARDC) [34]. In this benchmark experiment, the power coefficient of the scaled wind turbine was measured under different blade tip-speed ratios, providing a reference dataset for numerical validation [34]. The scaled NH1500 blade was treated as rigid in the present numerical validation, as previous aeroelastic analysis indicated that the structural deformation of the blade remained limited under the investigated conditions.

The benchmark case was performed at an incoming wind speed of 10.4 m/s and a rotational speed of 17.2 rpm, with zero yaw angle and zero blade pitch angle. The numerical results were compared with the experimental measurements in terms of the power coefficient $C_p$ at different blade tip-speed ratios. As shown in Fig. 2a, the CFD results reproduce the overall variation trend of the experimental $C_p$ curve. The maximum predicted power coefficient is 0.505 at a blade tip-speed ratio of 9.48, which is approximately 3% higher than the experimental maximum value of 0.49. Although slight discrepancies appear when the blade tip-speed ratio exceeds 11.5, the numerical results agree well with the experimental data over the main operating range. This comparison demonstrates that the CFD approach adopted in the present study can predict wind turbine aerodynamic performance with acceptable accuracy. It should be noted that this benchmark is used as a methodological validation of the CFD framework, including geometry-resolved modelling, solver settings, turbulence-model implementation and aerodynamic-force prediction. It is not regarded as a direct validation of the fully feathered parked turbine under strongly separated typhoon inflow; this limitation is considered when interpreting the subsequent full-scale results.

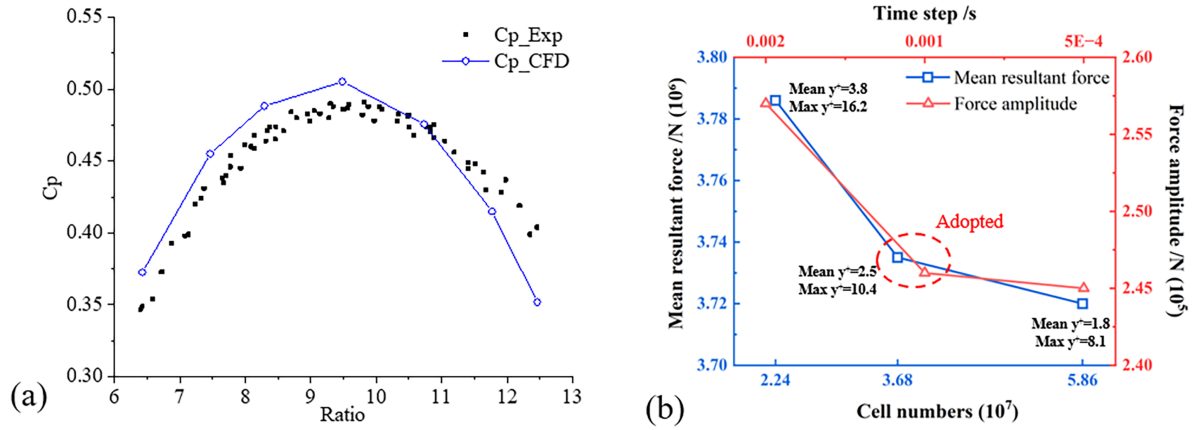



**Figure 2:** Validation of the numerical model and grid independence verification. (**a**) Comparison of experimental and numerical power coefficients of the NH1500 wind turbine at different blade tip-speed ratios [7]; (**b**) grid and time-step independence verification based on the mean resultant force and force amplitude.

In addition to the benchmark validation, grid and time-step independence were examined using the full parked-turbine model. As shown in Fig. 2b, three mesh levels with $2.24 \times 10^7$, $3.68 \times 10^7$, and $5.86 \times 10^7$ cells

were compared, together with time steps of 0.002 s, 0.001 s, and $5 \times 10^{-4}$ s. The west-inflow condition was selected for evaluating the mean resultant force because it produced the largest mean aerodynamic load among the eight inflow directions. The southeast-inflow condition was selected for evaluating the force-fluctuation amplitude because it produced the strongest unsteady load fluctuation. The mean resultant force and force amplitude changed only slightly after the intermediate mesh level. Therefore, the case with $3.68 \times 10^7$ cells and a time step of 0.001 s was adopted for the subsequent simulations as a compromise between numerical accuracy and computational cost. The near-wall mesh quality was also checked: the corresponding mean $y^+$ values were 3.8, 2.5, and 1.8, and the maximum $y^+$ values were 16.2, 10.4, and 8.1 for the coarse, intermediate, and fine meshes, respectively. Compared with the fine mesh, the intermediate mesh produced differences of only 0.43% in the west-inflow mean resultant force and 0.82% in the southeast-inflow force-fluctuation amplitude. These results indicate that the selected mesh and time step provide a stable compromise among overall cell number, near-wall resolution, and transient computational cost.

### *3.3 Mesh Generation*

To accurately capture the flow field around the ultra-large parked wind turbine while maintaining reasonable computational cost, a zonal mesh strategy was adopted in this study. The investigated turbine has a tower height of 130 m and a rotor diameter of 220 m, indicating that both the vertical structural scale and the rotor-swept region reach the hundred-meter level. Such a large geometric scale requires sufficient mesh resolution not only near the blade and tower surfaces, but also in the surrounding near-wake region where flow separation, velocity deficit and blade–tower interference may occur.

The outer computational domain was discretized using a structured mesh to provide a regular far-field grid and maintain numerical stability away from the turbine. Around the full turbine, including the blades, hub, nacelle and tower, a locally refined hexahedral mesh was generated to improve the resolution of near-body flow, surface pressure gradients, local separation and wake development. The refined region was arranged around the complete parked turbine rather than being limited to the immediate wall-adjacent region, because the 220 m rotor diameter and 130 m tower height enlarge the spatial range over which separated flow and wake interactions may develop. The mesh density was increased in the turbine-surrounding region and gradually reduced toward the far-field boundaries to avoid abrupt cell-size variation. This treatment reduces excessive numerical diffusion in the predicted separated flow around the parked blades and the velocity-deficit wake behind the tower. Similar near-body/background-domain partitioning has been adopted in recent geometry-resolved wind turbine CFD frameworks, where different mesh systems are used for the near-turbine and background-flow regions to balance geometric fidelity and computational efficiency [34].

The structured outer mesh and the refined inner hexahedral mesh were connected using the mesh interface technique in ANSYS Fluent. The mesh interface enables the transfer of flow variables and fluxes between adjacent mesh regions with different grid densities, thereby maintaining solution continuity across the interface. This strategy combines the numerical efficiency of the structured background mesh with the local resolution of the refined turbine-region mesh. The generated mesh was subsequently used for the grid-independence analysis and all whole turbine-simulations. The mesh layout is shown in Fig. 3. Fig. 3a presents the surface mesh of the outer computational domain, and Fig. 3b shows the overall zonal mesh arrangement with the inner refined region embedded in the structured background mesh. Fig. 3c shows the inner refined hexahedral mesh region and the mesh interface between the refined region and the surrounding background mesh. Fig. 3d presents the surface mesh of the full turbine, while Fig. 3e shows the local mesh details around the blade root, hub and tower-top junction, where geometric curvature and component connection effects require higher local mesh resolution.

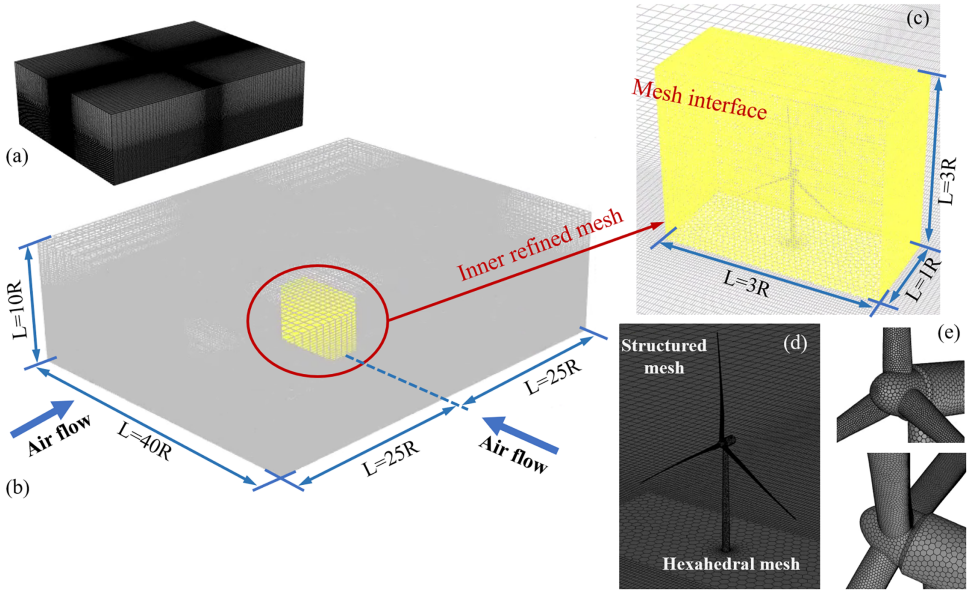



**Figure 3:** Mesh generation strategy for the full parked wind turbine: (**a**) surface mesh of the outer computational domain; (**b**) overall view of the zonal mesh arrangement, including the outer structured mesh and the inner refined region around the turbine; (**c**) inner refined hexahedral mesh region and mesh interface between the refined region and the background mesh; (**d**) mesh of the turbine surface; (**e**) local mesh details around the blade root, hub and tower-top junction.

## 4 Numerical Results and Discussion

In this section, the aerodynamic response of the full ultra-large parked wind turbine is analyzed under eight representative typhoon inflow directions. The turbine considered in this study has a tower height of 130 m and a rotor diameter of 220 m, and therefore the aerodynamic loading is expected to be strongly affected by the spatial distribution of pressure, separated flow around the parked blades, and the wake development behind the tower. All simulations are conducted for the complete turbine configuration, including the blades, hub, nacelle and tower, so that the aerodynamic characteristics can be evaluated at the whole turbine scale rather than from isolated components. The following analysis first compares the directional variation of the aerodynamic forces among the three blades and the entire rotor, and then examines representative flow-field contours to explain the physical origin of the observed load differences. Particular attention is paid to whether the pressure distribution, blade-section vortex patterns and tower velocity-deficit wake are consistent with the force distributions against inflow directions.

### *4.1 Overall Aerodynamic Response*

The directional aerodynamic response of the full parked wind turbine under eight typhoon inflow directions is shown in Fig. 4. As shown in Fig. 4f, the resultant aerodynamic force of the full turbine varies markedly with inflow direction, ranging from $2.214 \times 10^6$ N to $3.720 \times 10^6$ N. The largest whole turbine force occurs under the west inflow condition, reaching $3.720 \times 10^6$ N, followed by the east, northeast and northwest inflows, with values of $3.671 \times 10^6$ N, $3.391 \times 10^6$ N and $3.337 \times 10^6$ N, respectively. In contrast, the south and north inflow conditions produce much lower resultant forces of $2.214 \times 10^6$ N and $2.223 \times 10^6$ N. The southeast and southwest inflows show intermediate force levels, with resultant forces of $3.155 \times 10^6$ N and $3.188 \times 10^6$ N, respectively. It is indicated that the aerodynamic loading of the parked turbine is strongly direction-dependent, with west, east, northeast and northwest inflows representing the critical loading directions for the present parked posture.

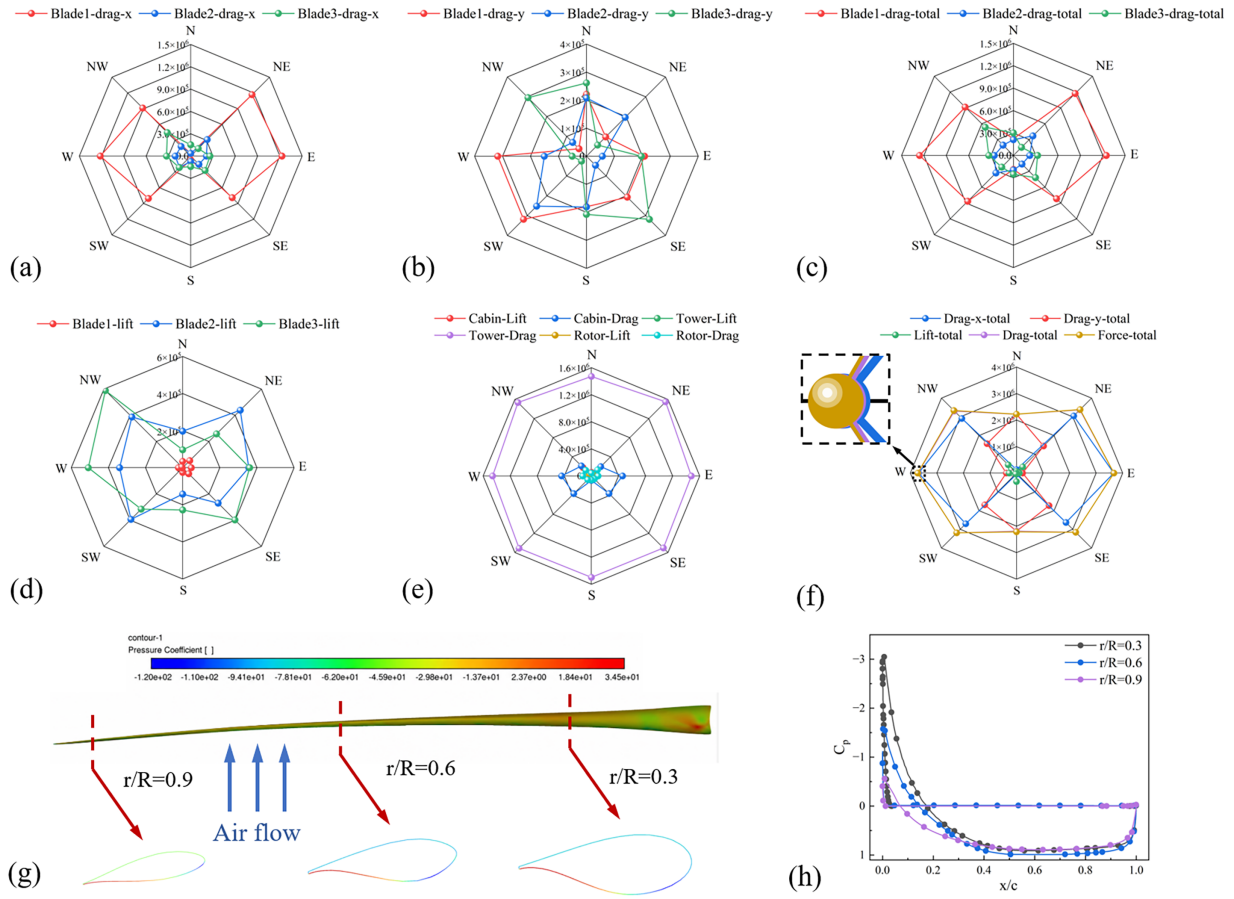



**Figure 4:** Directional aerodynamic response of the full parked wind turbine under eight typhoon inflow directions: (**a**) mean blade drag in the *x*-direction; (**b**) mean blade drag in the *y*-direction; (**c**) resultant drag of each blade; (**d**) mean lift of each blade; (**e**) lift and drag of the nacelle, tower and rotor; (**f**) drag, lift and resultant aerodynamic forces of the turbine; (**g**) surface pressure-coefficient distribution of Blade 1 and representative sectional pressure distributions at r/R = 0.3, 0.6, and 0.9 under east inflow; and (**h**) corresponding chordwise pressure-coefficient distributions at the three spanwise locations.

From the force composition shown in Fig. 4c–f, the resultant aerodynamic force is mainly governed by the resultant drag. Under west inflow, the resultant drag reaches $3.710 \times 10^6$ N, which is nearly identical to the total aerodynamic force of $3.720 \times 10^6$ N. Similar drag-dominated behavior is observed under east, northeast and northwest inflows, where the resultant drag reaches $3.669 \times 10^6$ N, $3.375 \times 10^6$ N and $3.308 \times 10^6$ N, respectively. It is indicated that the critical aerodynamic state of the parked turbine under extreme inflow is primarily controlled by drag loading. As shown in Fig. 4d, the lift contribution is generally smaller than the resultant drag, although its relative importance varies with wind direction. For instance, the total lift is only $2.75 \times 10^4$ N under west inflow, whereas it increases to $4.42 \times 10^5$ N under northwest inflow. This suggests that the force composition changes with inflow orientation, especially when the projected relationship between the blades and the incoming flow becomes less favorable for purely drag-dominated loading. In addition, Fig. 4e shows the same magnitude order of lift and drag of the nacelle, tower and rotor. The tower drag remains the dominant component among the three parts, with the order of $10^6$ N, while the nacelle and rotor forces show stronger directional variation. Therefore, the whole turbine aerodynamic response is not only determined by the rotor loads, but also strongly affected by the baseline drag contribution from the tower and the directional sensitivity of the nacelle. The separate drag components in Fig. 4f further show that

the total force is highly sensitive to the partition between drag-x-total and drag-y-total. East and west inflows are dominated by the $x$-direction drag component, whereas north and south inflows are mainly governed by the $y$-direction drag component; for oblique inflows, the simultaneous contribution of both components produces intermediate to high resultant forces.

The blade-resolved drag distributions in Fig. 4a,c reveal that the aerodynamic loads are not evenly shared by the three parked blades. Blade 1 carries the dominant drag in most high-load directions. Its resultant drag reaches $1.258 \times 10^6$ N under west inflow, $1.246 \times 10^6$ N under east inflow, and $1.172 \times 10^6$ N under northeast inflow. These values are substantially higher than those of Blade 2 and Blade 3 under the same directions, indicating that Blade 1 is the primary contributor to the extreme drag response of the rotor. By comparison, the maximum drag of Blade 2 occurs under northeast inflow, reaching $3.70 \times 10^5$ N, while Blade 3 reaches its maximum drag under northwest inflow, with a value of $5.35 \times 10^5$ N. Therefore, although Blade 1 dominates the overall drag level, Blade 2 and Blade 3 contribute noticeably under oblique inflow directions.

The lift distribution in Fig. 4d shows a different directional pattern from the drag distribution. Blade 1 produces relatively small lift in all directions, with its maximum lift being only $5.36 \times 10^4$ N under northeast inflow. In contrast, Blade 2 and Blade 3 exhibit much stronger lift responses. Blade 2 reaches its maximum lift of $4.38 \times 10^5$ N under northeast inflow, followed by $3.94 \times 10^5$ N under southwest inflow and $3.87 \times 10^5$ N under northwest inflow. Blade 3 produces the largest lift among the three blades, reaching $5.88 \times 10^5$ N under northwest inflow and $5.08 \times 10^5$ N under west inflow. These contrasts illustrate that the drag response is mainly dominated by Blade 1, whereas the lift response is more strongly associated with Blade 2 and Blade 3, particularly under oblique inflow conditions.

To further examine the surface-pressure characteristics of Blade 1, the east inflow condition was selected for detailed analysis. Under this condition, the whole-turbine resultant force reaches $3.671 \times 10^6$ N, while the resultant drag of Blade 1 reaches $1.246 \times 10^6$ N, making east inflow one of the critical loading directions considered in the present study. As shown in Fig. 4g, the pressure-coefficient distribution over Blade 1 exhibits evident spanwise variation. Representative sections at r/R = 0.3, 0.6, and 0.9 were therefore selected to further quantify the chordwise pressure characteristics. The corresponding chordwise distributions in Fig. 4h show that the main differences among the three sections are concentrated near the leading edge. The r/R = 0.3 section exhibits the strongest suction peak, followed by r/R = 0.6, whereas the suction peak at r/R = 0.9 is substantially weaker. Downstream of the leading-edge region, the pressure distributions gradually recover and become relatively smooth over most of the chord. These results indicate a clear spanwise redistribution of the blade-surface pressure under east inflow, with the inboard section experiencing a stronger leading-edge pressure gradient than the outboard sections.

The above results show that the aerodynamic loading of the three parked blades is highly dependent on inflow direction. However, the most critical direction for mean loading does not necessarily correspond to the strongest unsteady response. Therefore, the fluctuation amplitudes of the lift, drag, and resultant-force components were further examined. The initial transient stage was removed before the amplitude analysis, and the statistically stable portion of each force history was used. For consistency, the same statistical-window length was applied to all inflow directions. The fluctuation amplitude was calculated as the half peak-to-peak value:

$$A_F = \frac{(F_{max} - F_{min})}{2} \tag{5}$$

where $F_{max}$ and $F_{min}$ denote the maximum and minimum values of the corresponding force component within the selected stable interval. This definition allows the amplitude to characterize the post-transient unsteady load variation. As shown in Fig. 5, the amplitude distribution differs significantly from the

mean-force distribution shown in Fig. 4. While the mean resultant force is mainly dominated by west, east, northeast and northwest inflows, the strongest load fluctuation appears under the southeast inflow condition. The total drag amplitude reaches $2.43 \times 10^5$ N under southeast inflow, which is much higher than those under west inflow ($1.18 \times 10^5$ N), southwest inflow ($6.33 \times 10^4$ N), and south inflow ($4.48 \times 10^4$ N). The total lift amplitude also reaches its maximum value of $1.96 \times 10^5$ N under southeast inflow. This indicates that the inflow direction responsible for the largest mean load is not necessarily the same as that responsible for the strongest unsteady load fluctuation.

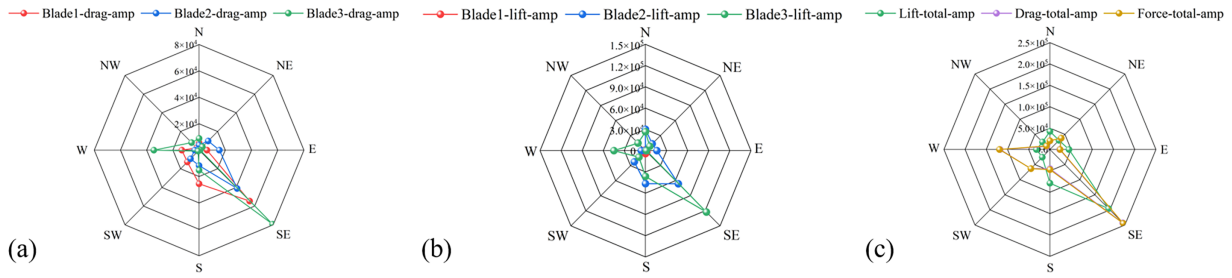



**Figure 5:** Amplitude of aerodynamic-force fluctuations of the full parked wind turbine under eight typhoon inflow directions: (**a**) drag amplitude of each blade; (**b**) lift amplitude of each blade; (**c**) total drag, lift and resultant-force amplitudes of the full turbine.

The blade-resolved drag-amplitude results in Fig. 5a show that the southeast inflow produces the strongest drag fluctuation on all three blades. The drag amplitudes of Blade 1, Blade 2 and Blade 3 under southeast inflow are $5.45 \times 10^4$ N, $4.11 \times 10^4$ N and $7.93 \times 10^4$ N, respectively. Among them, Blade 3 exhibits the largest drag-amplitude response, suggesting that the unsteady drag fluctuation is more pronounced on the lower blade rather than on Blade 1. Under west inflow, Blade 3 also shows a relatively high drag amplitude of $3.45 \times 10^4$ N, whereas Blade 1 and Blade 2 are lower, with amplitudes of $1.32 \times 10^4$ N and $3.34 \times 10^3$ N, respectively. This differs from the mean-force result, where Blade 1 dominates the drag load under west inflow. Therefore, the mean drag and drag fluctuation are controlled by different blade responses.

The lift-amplitude distribution in Fig. 5b further demonstrates that the unsteady lift response is mainly associated with Blade 2 and Blade 3. Blade 1 exhibits relatively small lift amplitudes in all inflow directions, with the relatively small maximum value of $4.29 \times 10^3$ N under south inflow. In contrast, Blade 3 reaches a lift amplitude of $1.23 \times 10^5$ N under southeast inflow, which is the largest single-blade lift fluctuation among all cases. Blade 2 also shows a high lift amplitude under southeast inflow, reaching $6.62 \times 10^4$ N, followed by $4.66 \times 10^4$ N under south inflow. It is indicated that the fluctuation of lift is mainly governed by the lower blades, especially Blade 3 and Blade 2, although mean drag is dominated by Blade 1.

The total-force-amplitude results in Fig. 5c confirm the above trend. The whole turbine force amplitude reaches the maximum under southeast inflow, with a value of $2.45 \times 10^5$ N. The southwest and south inflows show lower but still noticeable force amplitudes of $6.34 \times 10^4$ N and $4.71 \times 10^4$ N, respectively. By contrast, the northwest inflow produces the smallest total force amplitude, approximately $1.16 \times 10^4$ N. This suggests that southeast inflow should be regarded as a critical direction for unsteady load fluctuation, even though it is not the most critical direction in terms of mean aerodynamic force.

The dominant frequencies of the aerodynamic-force fluctuations are further compared in Fig. 6 to identify the characteristic time scales of the unsteady loads. Different from the force-amplitude distribution in Fig. 5, the frequency response does not concentrate only in the southeast inflow condition, but varies among blades and turbine components. For the lift frenquency response, Blade 1 reaches the highest dominant frequency under the north inflow condition, with a value of 5.797 Hz. Blade 3 exhibits

a pronounced lift-frequency response under southeast inflow, with a dominant frequency of 2.484 Hz, whereas Blade 2 exhibits a dominant frequency of 1.242 Hz under the same inflow direction. This frequency distribution indicates that the strongest force amplitude and the highest dominant frequency are not necessarily associated with the same blade or inflow direction.

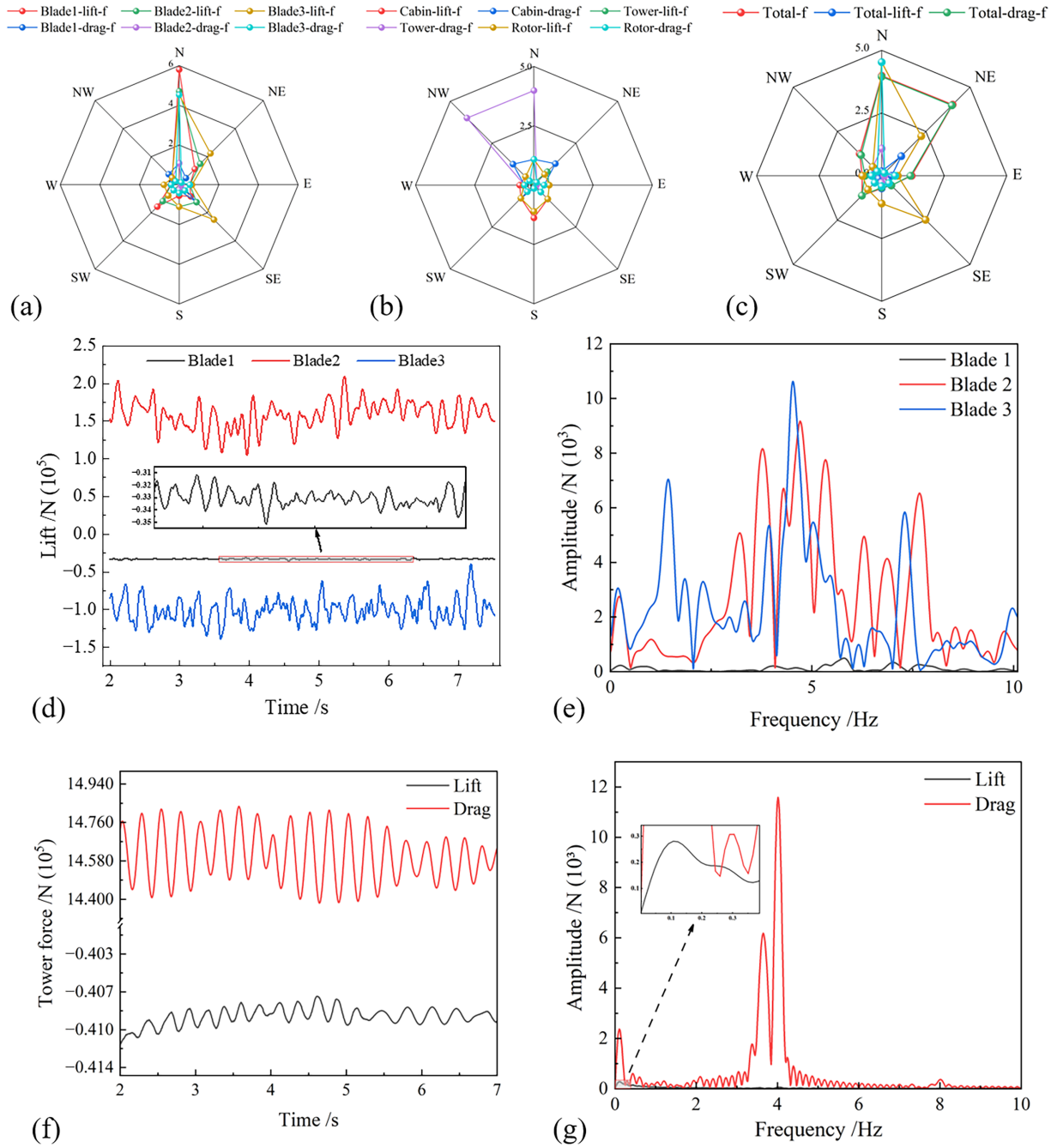



**Figure 6:** Dominant frequencies of aerodynamic force fluctuations under typhoon inflow directions: (**a**) dominant lift and drag frequencies of the three blades; (**b**) dominant lift and drag frequencies of the nacelle, tower and rotor components; (**c**) dominant total lift and drag frequencies of the three blades. Under the N inflow direction: (**d**) lift histories of each blade; (**e**) lift-frequency spectra of each blade; (**f**) tower lift and drag histories; (**g**) frequency spectra of tower lift and drag.

For the drag-frequency response, Blade 3 under north inflow exhibits the highest value among the blade drag components, reaching 4.529 Hz. Blade 1 also shows a relatively high drag frequency under southeast inflow, reaching 1.242 Hz, while the corresponding drag frequencies of Blade 2 and Blade 3 under southeast inflow are both 0.414 Hz. Therefore, the southeast inflow produces the strongest aerodynamic-force amplitude, but its dominant frequency remains mainly in the low-frequency range for the total rotor response. This feature is important for ultra-large parked wind turbines, because low-frequency load fluctuations can be more relevant to large-scale structural vibration and fatigue accumulation than high-frequency local fluctuations.

The component-level frequency results in Fig. 6b show that the tower-related response also varies strongly with inflow direction. The tower drag frequency reaches 3.999 Hz under northwest inflow and 3.986 Hz under north inflow, while the tower lift frequency reaches 0.1068 Hz under north inflow. The tower-drag frequencies are higher than most rotor-scale frequencies, whereas the tower lift response under north inflow is concentrated at a much lower frequency. For the rotor-scale response in Fig. 6c, the dominant lift frequency reaches 1.106 Hz under south inflow and 1.087 Hz under north inflow, whereas the rotor drag frequency reaches 1.087 Hz under north inflow. Under southeast inflow, the rotor lift and drag frequencies are 0.828 and 0.414 Hz, respectively. Thus, although the southeast inflow produces the largest force amplitude, its rotor-scale response is dominated by relatively low frequencies, indicating that the strong load fluctuation is mainly associated with low-frequency full-turbine unsteadiness rather than high-frequency component-level oscillation.

For the representative N inflow condition, the time-domain and frequency-domain responses are further shown in Fig. 6d–g. The lift histories and lift-frequency spectra of the three blades in Fig. 6d,e reveal the blade-resolved unsteady lift response. In comparison, the tower lift-drag histories and tower lift-drag spectra in Fig. 6f,g show that the tower drag contains a pronounced spectral peak near 4 Hz, whereas the tower lift is mainly concentrated at a much lower frequency. These subfigures provide direct time-series and spectral evidence for the frequency characteristics summarized in Fig. 6a–c.

Overall, Figs. 4–6 reveal pronounced directional asymmetry in the mean loads, fluctuation amplitudes and dominant frequencies of the whole turbine. For the mean aerodynamic loads, west and east inflows produce the strongest drag-dominated states, while northeast and northwest inflows also generate high resultant forces with noticeable lift contributions from the lower blades. For the fluctuating loads, the dominant direction changes: southeast inflow produces the largest aerodynamic-force amplitude, although its mean resultant force is not the maximum. For the frequency response, north inflow produces the highest blade lift frequency on Blade 1 and the highest drag frequency on Blade 3, while northwest inflow induces a high tower drag frequency. Therefore, west and east inflows are more critical for extreme mean loading, southeast inflow is more critical for load-amplitude amplification, and north/northwest inflows are more relevant to high-frequency component-level responses. For ultra-large parked wind turbines with hundred-meter-scale blades and high towers, critical inflow directions should be identified by combining mean loads, fluctuation amplitudes and dominant frequency characteristics. The directional load redistribution, amplitude amplification and frequency response provide the quantitative basis for the flow-field interpretation in the following section.

### *4.2 Tower-Blade Interaction and Wake Analysis*

The aerodynamic-force results in Section 4.1 show clear directional differences in the mean load, fluctuation amplitude and dominant frequency of the parked wind turbine. To further identify the flow-field origin of these differences, the surface pressure contours of the full turbine, blade-section Q-criterion vortex distributions, and tower velocity are further discussed. Based on the load characteristics discussed

above, south, west and southeast inflows are selected as three representative cases, corresponding to a low mean-load state, an extreme mean-load state and a strong fluctuation-amplitude state, respectively. The comparative analysis of these three cases further links pressure concentration, blade-section vortex structures and tower-wake morphology to the directional aerodynamic-load characteristics of the ultra-large parked wind turbine.

Under the south inflow condition, the whole turbine resultant force is $2.214 \times 10^6$ N, corresponding to the lowest mean-load state among the examined inflow directions. As indicated by the inflow-direction schematic in Fig. 7f, the incoming flow approaches the parked turbine from the south side, resulting in a relatively dispersed exposure of the three stationary blades to the wind. This feature is consistent with the relatively scattered pressure distribution shown in Fig. 7a, where exhibits a dispersed loading pattern, with no continuous high-pressure region formed on any individual blade. This illustrates that the aerodynamic load in this case is not dominated by a single strongly exposed blade. It agrees well with the blade-resolved force results, since the drag forces of Blade 1, Blade 2 and Blade 3 are $1.87 \times 10^5$ N, $1.95 \times 10^5$ N and $2.51 \times 10^5$ N, respectively, remaining at the same order of magnitude.

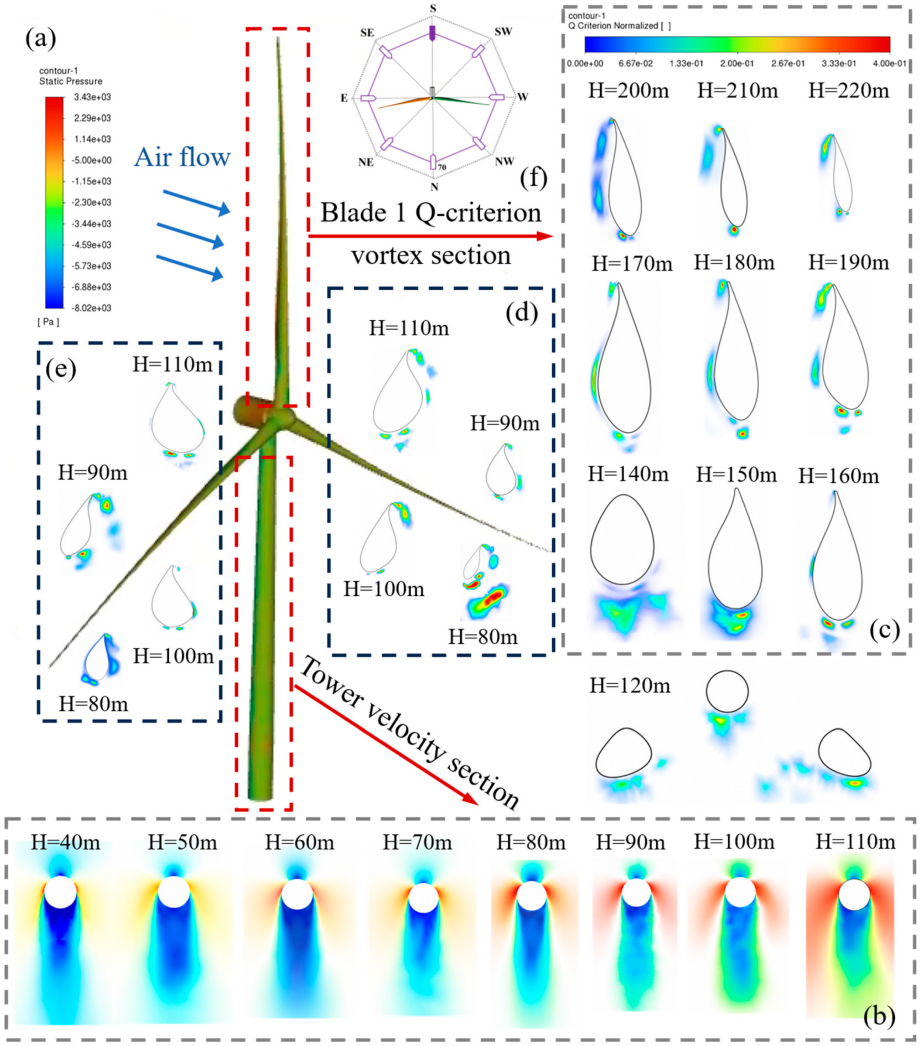



**Figure 7:** Flow-field characteristics of the parked wind turbine under the south inflow condition: (**a**) surface pressure distribution on the full turbine; (**b**) tower velocity sections; (**c**–**e**) Q-criterion vortex structures around Blades 1, 2 and Blade 3; (**f**) schematic of the south inflow direction.

The Q-criterion sections further illustrate the moderate loading level under this inflow direction. As shown in Fig. 7c, the sections around Blade 1 at different heights are mainly characterized by localized and discrete vortex patches, without showing continuously intensified separation over multiple height sections, indicating that Blade 1 does not induce strong separated vortices. In Fig. 7d, the sectional vortex structures around Blade 2 are also relatively weak and localized. Although separated vortices appear at some heights, the vortex cores remain small, which is consistent with the similar drag levels of Blade 1 and Blade 2. In Fig. 7e, slightly stronger vortex concentration appears at some height sections around Blade 3, corresponding to its higher drag, but still without a strong separation pattern that intensifies simultaneously across multiple height sections. Meanwhile, the tower velocity sections Fig. 7b show a relatively organized velocity-deficit wake behind the tower, especially in the lower and middle tower regions. Near the nacelle and blade-root region, the wake becomes wider and slightly distorted, but the vortex-coupling effect between the blades and the tower remains limited. Therefore, the weaker pressure concentration in Fig. 7a, the more scattered sectional vortex patterns in Fig. 7c–e, and the relatively organized tower wake in Fig. 7b together illustrate the lower resultant force under the south inflow condition.

Under the west inflow condition, the aerodynamic loading increases significantly. The whole turbine resultant force reaches $3.720 \times 10^6$ N, while the total drag reaches $3.710 \times 10^6$ N, indicating a typical drag-dominated extreme loading state. As shown in Fig. 8f, the incoming flow approaches the parked turbine from the west side, making Blade 1 more directly exposed to the incoming flow than in the south inflow case. The pressure contours in Fig. 8a show a large pressure difference between the windward and leeward sides of Blade 1. Compared with the south inflow case shown in Fig. 8a, reveal a pronounced pressure contrast across Blade 1, with the high-pressure region extending over its main windward surface. Compared with the south inflow case, the pressure loading becomes more concentrated on Blade 1 rather than remaining locally distributed around the tower and nacelle. This pressure concentration directly corresponds to the force results, where the drag of Blade 1 reaches $1.26 \times 10^6$ N, much larger than those of Blade 2 and Blade 3, which are $2.57 \times 10^5$ N and $3.30 \times 10^5$ N, respectively. Therefore, the maximum resultant force under west inflow is mainly caused by the strong pressure loading and enhanced separated-flow around Blade 1.

The Q-criterion sections of Blade 1 shown in Fig. 8c further reveal the separated-flow characteristics under the west inflow condition. Distinct vortex-concentration regions appear at multiple spanwise sections, and their morphology varies noticeably along the blade. Moving upward along the blade, the separated vortices initially remain relatively localized near the blade section. Further upward, the vortex regions expand and develop into more elongated structures extending away from the blade surface. Toward the upper part of the blade, the vortex field becomes more dispersed, with multiple separated vortex patches distributed around the section. Such variations in vortex size, shape, and spatial distribution demonstrate the pronounced spanwise non-uniformity of the separated flow around Blade 1.

The vortex structures of Blade 2 and Blade 3 in Fig. 8d,e also reflect the influence of this high-load condition on the downstream blades. In Fig. 8d, the vortex structures around Blade 2 are weaker than those around Blade 1, but stretched or displaced vortex patches can still be observed at some heights, indicating that the local inflow around Blade 2 is disturbed by upstream blade separation, nacelle flow and the tower velocity-deficit region. Since Blade 2 is not the primary windward blade under this inflow direction, its sectional vortex structures do not exhibit the same persistently strong separation as those of Blade 1, which is consistent with its smaller drag contribution. By contrast, the local vortex structures around Blade 3 in Fig. 8e are more evident than those around Blade 2, and stronger vortex concentration appears in several sections. This agrees with its relatively large drag and high lift of $5.08 \times 10^5$ N. It is indicated that although Blade 3 is not the primary drag-bearing blade, its local inflow direction is altered by the deflected wake, resulting in an asymmetric surface-pressure distribution and a pronounced lift response. Therefore, the risk associated with the west

inflow condition is not limited to the extreme drag on Blade 1, but also involves asymmetric aerodynamic loading on downstream blades induced by the coupling between blade separation and the tower wake.

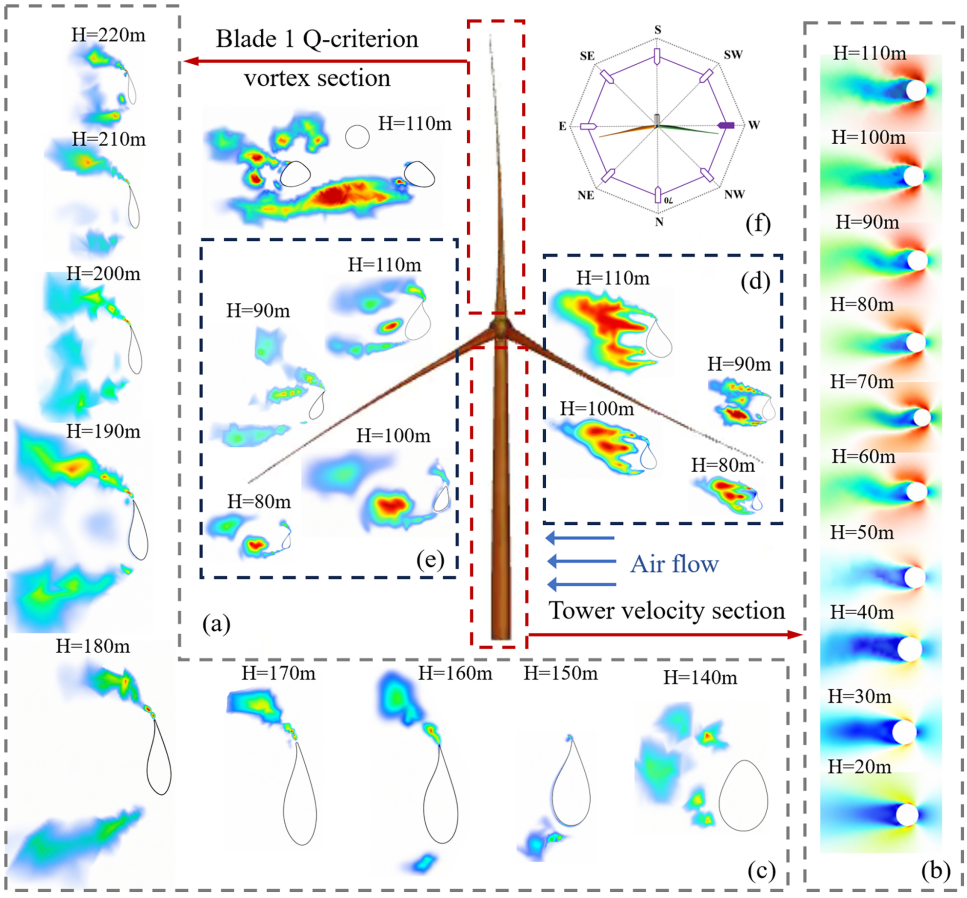



**Figure 8:** Flow-field characteristics of the full parked wind turbine under the west inflow condition: (**a**) surface pressure distribution on the full turbine; (**b**) tower velocity sections showing the vertical evolution of the velocity-deficit wake; (**c**–**e**) Q-criterion vortex distributions around Blades 1, 2 and 3; (**f**) schematic of the west inflow direction.

Under the southeast inflow condition, the whole turbine mean resultant force is not the maximum among the eight inflow directions, but the aerodynamic-force fluctuation becomes the strongest. This behavior is consistent with the amplitude results in Section 4.1, where the total force amplitude, drag amplitude and lift amplitude all reach their maximum values under southeast inflow. As shown in Fig. 9g, the incoming flow approaches the parked rotor from an oblique direction. This inflow orientation does not produce the strongest frontal loading on Blade 1 as in the west inflow case, but it changes the local inflow condition of the lower blades and enhances the unsteady interaction among blade-separated vortices, tower wake and local velocity deficit.

The surface pressure distribution in Fig. 9a shows an asymmetric pressure pattern on the full turbine. The pressure difference is not concentrated only on the upper blade; instead, the pressure-loaded regions are redistributed among the blades and the tower-facing region. This pressure redistribution corresponds to the force-amplitude characteristics discussed in Section 4.1, where southeast inflow produces strong temporal fluctuations in both drag and lift despite its non-maximum mean resultant force. The Q-criterion sections of Blade 1 in Fig. 9c show vortex-concentration regions at several heights, but these sectional vortices

are less dominant than those around Blade 1 under west inflow. Therefore, Blade 1 is not the sole source of the unsteady response in this case. The Q-criterion sections around Blade 2 and Blade 3 in Fig. 9d,e are more important for explaining the large fluctuation amplitude under southeast inflow. In Fig. 9d, the vortices around Blade 2 appear at multiple height sections and show evident spatial variation, indicating that Blade 2 experiences a strongly non-uniform local inflow. In Fig. 9e, Blade 3 also exhibits distinct vortex-concentration regions, especially at the lower-height sections. These sectional vortex features are consistent with the amplitude results discussed in Section 4.1, where Blade 3 contributes most strongly to drag and lift fluctuations under southeast inflow, and Blade 2 also shows a large lift amplitude. The strong load fluctuation under southeast inflow is therefore associated with the combined unsteady response of Blade 2 and Blade 3, rather than a mean load mechanism dominated by Blade 1. The tower velocity sections in Fig. 9b further show that the wake behind the tower is not simply aligned with the tower centerline. The velocity-deficit region is deflected and distorted along the downstream direction, indicating that the tower wake interacts with the oblique inflow and the blade wake. The additional velocity and vorticity contours on the H = 120 m cross-section in Fig. 9f provide a clearer view of this local interaction near the upper tower and rotor region.

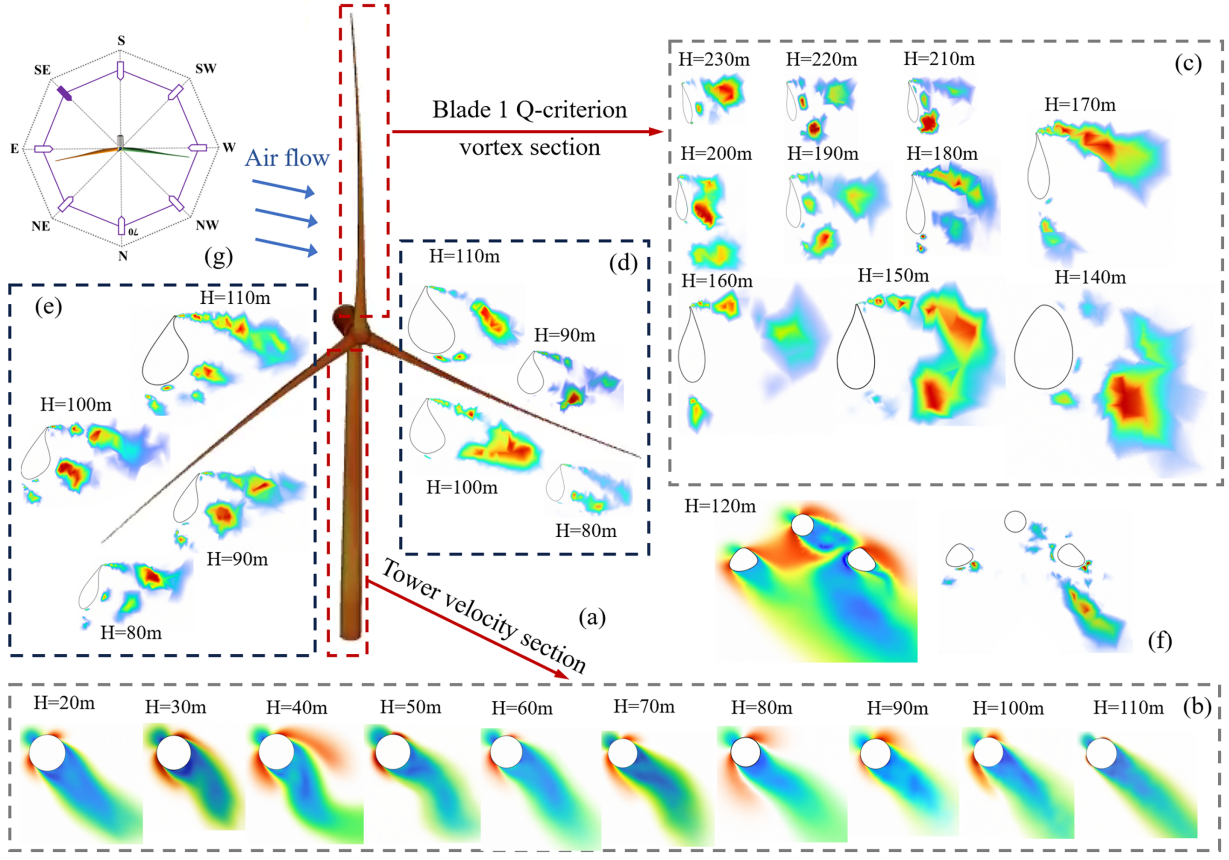



**Figure 9:** Flow-field characteristics of the full parked wind turbine under the southeast inflow condition: (**a**) surface pressure distribution on the full turbine; (**b**) tower velocity sections at different heights; (**c**–**e**) Q-criterion vortex structures around Blade 1, 2 and 3 at different heights; (**f**) velocity and vorticity contours on the H = 120 m cross-section; (**g**) schematic of the southeast inflow direction.

These flow features explain why the southeast inflow produces the strongest aerodynamic-force fluctuation. The oblique inflow redistributes the local separation and wake interaction among the lower blades and tower region, resulting in enhanced unsteady load oscillation at the whole turbine scale.

Overall, the representative flow-field results reveal the aerodynamic mechanisms underlying the directional load characteristics identified in Section 4.1. Under south inflow, the pressure field is relatively dispersed, the blade section vortices remain weak, and the tower wake maintains a more ordered velocity deficit, which together correspond to the low mean load state. Under west inflow, the large pressure difference on Blade 1 and the pronounced separated vortices in its Q-criterion sections support the drag response dominated by Blade 1 and the maximum mean resultant force. Under southeast inflow, the oblique incoming flow redistributes the local pressure loading and separated-vortex patterns among the lower blades and the tower-adjacent region. The velocity and vorticity contours on the H = 120 m section further show local velocity deficit and vortex concentration near the tower–rotor interaction region, which is consistent with the strongest aerodynamic-force fluctuation observed in Section 4.1. Therefore, for an ultra-large parked wind turbine with a 220 m rotor diameter and a 130 m tower height, the critical aerodynamic state is governed not only by the magnitude of the mean resultant force, but also by the coupled effects of pressure redistribution, blade-sectional separation, tower wake development and load-fluctuation amplitude. These results highlight the necessity of evaluating typhoon-induced aerodynamic risk from both mean-load and unsteady-fluctuation perspectives. From an engineering perspective, the west and east inflow cases are more relevant to ultimate mean-load checks, whereas the southeast inflow case should be considered in unsteady-load amplification and fatigue-related assessments. The tower region requires attention to tower-base bending moment, while the blade-root and nacelle-yaw connection regions require attention to load redistribution and oblique-inflow interference.

To provide an external load-scale reference, the present parked-state loads are also compared with publicly available data from the IEA Wind 15-MW reference wind turbine [35]. This turbine has a rotor diameter of 240 m and a hub height of 150 m, which are comparable in scale to the 220 m rotor diameter and 130 m tower height considered in the present study. Its rated wind speed is 10.59 m/s and the design thrust coefficient is approximately 0.804. Based on the standard rotor-thrust relation, the rated operating rotor thrust is on the order of $2.5 \times 10^6$ N. In comparison, the maximum whole-turbine resultant force in the present parked extreme-wind simulations reaches $3.720 \times 10^6$ N, and the maximum force-fluctuation amplitude reaches $2.45 \times 10^5$ N. Because the turbine geometry, control state, and inflow condition differ, this comparison should not be interpreted as a strict validation. Nevertheless, it provides an external order-of-magnitude load reference, indicating that the predicted parked-state aerodynamic loads are within a physically reasonable load scale for ultra-large offshore wind turbines under extreme wind conditions. The same public reference also shows that yaw-misaligned parked conditions with extreme wind speeds can appear among the worst-case load scenarios in IEC design-load-case analysis, further supporting the engineering relevance of the present parked extreme-wind analysis [35].

## 5 Conclusions

In this study, whole-turbine unsteady CFD simulations were conducted to investigate the aerodynamic characteristics of an ultra-large parked wind turbine under representative directional extreme-wind conditions. The investigated turbine has a tower height of 130 m and a rotor diameter of 220 m. A fixed-azimuth, fully feathered, and braked parked configuration was considered. Eight representative inflow directions were considered to examine the directional dependence of mean aerodynamic loads, fluctuation amplitudes, dominant frequencies, and representative flow-field structures. The main conclusions are as follows:

1. The mean aerodynamic load of the ultra-large parked wind turbine shows pronounced directional dependence under the fixed parked configuration. Among the eight inflow directions, west inflow produces the largest whole-turbine resultant force, reaching $3.720 \times 10^6$ N. East, northeast and northwest inflows also generate relatively high resultant forces of $3.671 \times 10^6$ N, $3.391 \times 10^6$ N and $3.337 \times 10^6$ N, respectively, whereas south and north inflows produce much lower mean loads. Therefore, for the present fully feathered and braked parked posture, west, east, northeast and northwest inflows are the main critical directions in terms of extreme mean aerodynamic loading. This indicates that the fixed-azimuth parked condition can provide a clear reference case for identifying direction-dependent extreme load paths, although it does not represent all possible parked rotor positions.
2. The mean aerodynamic response is mainly drag-dominated, and the key load-bearing components differ among inflow directions. Under west inflow, the resultant drag reaches $3.710 \times 10^6$ N, which is nearly identical to the total aerodynamic force. Similar drag-dominated behavior is also observed under east, northeast and northwest inflows. At the blade level, Blade 1 contributes most strongly to the extreme drag response, especially under west, east and northeast inflows, while Blade 2 and Blade 3 provide more pronounced lift contributions under oblique inflow directions. At the component level, the tower drag forms the dominant baseline load of the full turbine, whereas the nacelle and rotor forces introduce additional wind-direction sensitivity. These results suggest that tower-base bending moment, blade-root loading, nacelle/yaw-system loading, and blade-tower interaction should be considered as key concerns in parked-state structural assessment under extreme wind conditions.
3. The fluctuation amplitude of aerodynamic loads exhibits a different directional pattern from the mean force. Although west and east inflows dominate the extreme mean drag response, southeast inflow produces the strongest unsteady load fluctuation. Under southeast inflow, the whole-turbine resultant-force amplitude reaches $2.45 \times 10^5$ N, while the total drag and lift amplitudes reach $2.43 \times 10^5$ N and $1.96 \times 10^5$ N, respectively. Thus, the wind direction associated with the maximum mean load is not necessarily the same as that associated with the strongest aerodynamic fluctuation. Therefore, southeast inflow should be considered a critical direction for unsteady load amplification and fatigue-related load evaluation, rather than being judged only from the mean aerodynamic force.
4. The critical aerodynamic state of an ultra-large parked wind turbine should be evaluated by combining mean load, load fluctuation and dominant-frequency characteristics. West and east inflows are more critical for extreme mean loading, southeast inflow is more critical for unsteady load amplification, while north and northwest inflows are associated with relatively high frequency responses in specific blade and tower components. The flow-field analysis further indicates that pressure concentration, blade-sectional separation, tower wake development, and blade-nacelle-tower interference jointly control the directional load redistribution. The parked-state safety assessment under typhoon conditions should not rely only on the maximum mean aerodynamic force, but should also consider force-amplitude amplification, dominant-frequency response, directional load redistribution, unsteady fluctuation and flow-induced interaction among the blades, nacelle and tower.

Overall, for an ultra-large parked wind turbine with a 220 m rotor diameter and a 130 m tower height, the critical aerodynamic state is governed by the combined effects of mean pressure loading, unsteady force-amplitude amplification, dominant-frequency response, blade-sectional separation and tower wake development. Typhoon-resistant assessment and parked-state safety design should therefore consider mean loads, fluctuation amplitudes and frequency characteristics simultaneously, rather than relying only on the maximum mean aerodynamic force. The present results provide a fixed-azimuth CFD reference for understanding the directional load characteristics of a fully feathered and braked parked turbine under extreme mean-wind conditions. They can support typhoon-resistant design, parked-state safety evaluation, and the identification of critical load paths for ultra-large wind turbines.

The present analysis also has some limitations associated with the adopted inflow specification and parked-state treatment. Extreme typhoon wind conditions are modeled using only a representative constant mean wind speed and eight typical fixed inflow directions, rather than through a full reconstruction of the complex spatiotemporal evolution of an actual typhoon boundary layer. In addition, the simulations mainly consider the turbine after blade feathering and rotor braking have been completed; consequently, the transient aerodynamic responses associated with the transition from operation to the parked state, including blade feathering, rotor braking, and rotor locking, are not fully accounted for. Future work will further investigate more realistic non-stationary typhoon inflow conditions and the transient aerodynamic evolution of the turbine during the shutdown and rotor-locking processes.

**Acknowledgement:** The authors would like to thank all those who have reviewed and contributed to this paper for their valuable assistance.

**Funding Statement:** This work was supported by the Central Government Guided Local Science and Technology Development Fund Projects (Grant No. 2025ZY01009; recipient: Ruiliang Wang), funded by the Zhejiang Provincial Department of Science and Technology (https://kjt.zj.gov.cn/).

**Author Contributions:** The authors confirm their contributions to the paper as follows: study conception and design: Congbo Zheng, Qian Chen and Ruiliang Wang; data collection: Congbo Zheng, Tianyu Song, Dongliang Yu and Di Tang; analysis and interpretation of results: Congbo Zheng, Qian Chen, Zeshuai Chen, Tianyu Song and Ruiliang Wang; draft manuscript preparation: Congbo Zheng, Chaojin Chen and Tianyu Song. All authors reviewed and approved the final version of the manuscript.

**Availability of Data and Materials:** The original test data for the experiment cannot be publicly shared per research confidentiality constraints, so the supporting data are not provided.

**Ethics Approval:** Not applicable.

**Conflicts of Interest:** The authors declare no conflicts of interest.

## References

1. Global Wind Energy Council. Global wind report 2026. Brussels, Belgium: Global Wind Energy Council; 2026 [cited 2026 Aug 20]. Available from: https://www.gwec.net/reports/globalwindreport.
2. International Renewable Energy Agency. Renewable capacity statistics 2026. Abu Dhabi, United Arab Emirates: International Renewable Energy Agency; 2026 [cited 2026 Aug 20]. Available from: https://www.irena.org/Publications/2026/Mar/Renewable-capacity-statistics-2026.
3. Li Z, Song L, Ma H, Xiao J, Wang K, Chen L. Observed surface wind speed declining induced by urbanization in east China. Clim Dyn. 2018;50(3–4):735–49. doi:10.1007/s00382-017-3637-6.
4. Yang H, Chen J, Pang X. Wind Turbine optimization for minimum cost of energy in low wind speed areas considering blade length and hub height. Appl Sci. 2018;8(7):1202. doi:10.3390/app8071202.
5. Ribnitzky D, Berger F, Petrović V, Kühn M. Hybrid-lambda: a low-specific-rating rotor concept for offshore wind turbines. Wind Energy Sci. 2024;9(2):359–83. doi:10.5194/wes-9-359-2024.
6. GB/T 19201—2006 Grade of Tropical Cyclones. General administration of quality supervision, inspection and quarantine of the People's Republic of China; Standardization administration of the People's Republic of China. Beijing, China: Standards Press of China; 2006 [cited 2026 Aug 20]. Available from: https://openstd.samr.gov.cn/bzgk/std/newGbInfo?hcno=016555C8A7A7F9EDDF96CE84A88EAFC6.
7. Tang D, Xu M, Mao J, Zhu H. Unsteady performances of a parked large-scale wind turbine in the typhoon activity zones. Renew Energy. 2020;149(2):617–30. doi:10.1016/j.renene.2019.12.042.

8. IEC 61400-1:2019+AMD1:2025 CSV. Wind energy generation systems—part 1: design requirements. Geneva, Switzerland: International Electrotechnical Commission; 2025 [cited 2026 Aug 20]. Available from: https://webstore.iec.ch/en/publication/111042.
9. Wang H, Wang T, Ke S, Hu L, Xie J, Cai X, et al. Assessing code-based design wind loads for offshore wind turbines in China against typhoons. Renew Energy. 2023;212(4):669–82. doi:10.1016/j.renene.2023.05.052.
10. Zhao Y, Tao Y, Chen Y, Yan J, Zeng Z. Increasing extreme winds challenge offshore wind energy resilience. Nat Commun. 2025;16(1):9529. doi:10.1038/s41467-025-65105-3.
11. Li Z, Chen S, Ma H, Feng T. Design defect of wind turbine operating in typhoon activity zone. Eng Fail Anal. 2013;27:165–72. doi:10.1016/j.engfailanal.2012.08.013.
12. Lian J, Jia Y, Wang H, Liu F. Numerical study of the Aerodynamic loads on offshore wind Turbines under Typhoon with full wind direction. Energies. 2016;9(8):613. doi:10.3390/en9080613.
13. Chou JS, Ou YC, Lin KY, Wang ZJ. Structural failure simulation of onshore wind turbines impacted by strong winds. Eng Struct. 2018;162:257–69. doi:10.1016/j.engstruct.2018.02.006.
14. Chou JS, Ou YC, Lin KY. Collapse mechanism and risk management of wind turbine tower in strong wind. J Wind Eng Ind Aerodyn. 2019;193:103962. doi:10.1016/j.jweia.2019.103962.
15. Wu L, Yu R, Xiang C, Yu H, Feng Y, Zhou X. Extreme impacts of four landfalling tropical Cyclones in China during the 2024 peak season. Adv Atmos Sci. 2025;42(5):817–24. doi:10.1007/s00376-025-4465-y.
16. ESCAP/WMO Typhoon Committee. Member report [China]. In: 20th Integrated Workshop; 2025 Dec 2–5; Macao, China [cited 2026 Aug 20]. Available from: https://typhooncommittee.org/20IWS/docs/Members%20REport/CHina/Member%20Report%20of%20China%20for%20Typhoon%20Committee%20IWS20.pdf.
17. Masters FJ, Vickery PJ, Bacon P, Rappaport EN. Toward objective, standardized intensity estimates from surface wind speed observations. Bull Am Meteorol Soc. 2010;91(12):1665–82. doi:10.1175/2010BAMS2942.1.
18. Song L, Chen W, Wang B, Zhi S, Liu A. Characteristics of wind profiles in the landfalling typhoon boundary layer. J Wind Eng Ind Aerodyn. 2016;149(10):77–88. doi:10.1016/j.jweia.2015.11.008.
19. Yi G, Pan J, Zhao L, Song L, Fang G, Cui W, et al. Profiles of mean wind and turbulence intensity during strong typhoon landfall. J Wind Eng Ind Aerodyn. 2022;228(1):105106. doi:10.1016/j.jweia.2022.105106.
20. Li J, Li Z, Jiang Y, Tang Y. Typhoon resistance analysis of offshore wind Turbines: a review. Atmos. 2022;13(3):451. doi:10.3390/atmos13030451.
21. Chen X, Li C, Xu J. Failure investigation on a coastal wind farm damaged by super typhoon: a forensic engineering study. J Wind Eng Ind Aerodyn. 2015;147(3):132–42. doi:10.1016/j.jweia.2015.10.007.
22. Chen X, Xu JZ. Structural failure analysis of wind turbines impacted by super typhoon Usagi. Eng Fail Anal. 2016;60(3):391–404. doi:10.1016/j.engfailanal.2015.11.028.
23. Jang JJ, Chien CW. Damage caused by typhoon and design of wind turbine towers. In: Proceedings of the ISOPE International Ocean and Polar Engineering Conference; 2010 Jun 20–26; Beijing, China. ISOPE-I-10-067. [cited 2026 Aug 20]. Available from: https://publications.isope.org/proceedings/ISOPE/ISOPE%202010/data/papers/10LKC-01Jang.pdf.
24. Glienke R, Kalkowsky F, Hobbacher A, Holch A, Ripsch B, Günther HP, et al. Improving the fatigue strength of butt welds in the as-welded and grit-blasted condition for steel towers of wind Turbines. Int J Offshore Polar Eng. 2024;34(2):199–209. doi:10.17736/ijope.2024.jc928.
25. Jonkman JM, Buhl ML Jr. FAST user's guide—updated august 2005. Golden, CO, USA: National Renewable Energy Laboratory; 2005. Report No.: NREL/TP-500-38230. doi:10.2172/15020796.
26. Moriarty PJ, Hansen AC. AeroDyn theory manual. Golden, CO, USA: National Renewable Energy Laboratory; 2005. Report No.: NREL/TP-500-36881. doi:10.2172/15014831.
27. Menter FR. Two-equation eddy-viscosity turbulence models for engineering applications. AIAA J. 1994;32(8):1598–605. doi:10.2514/3.12149.
28. Sørensen NN, Michelsen JA, Schreck S. Navier–stokes predictions of the NREL phase VI rotor in the NASA Ames 80 ft × 120 ft wind tunnel. Wind Energy. 2002;5(2–3):151–69. doi:10.1002/we.64.
29. Smagorinsky J. General circulation experiments with the primitive equations: I. the basic experiment. Mon Weather Rev. 1963;91(3):99–164. doi:10.1175/1520-0493(1963)091<0099:GCEWTP>2.3.CO;2.

30. Spalart PR, Jou WH, Strelets M, Allmaras SR. Comments on the feasibility of LES for wings and on a hybrid RANS/LES approach. In: Liu C, Liu Z, editors. Advances in DNS/LES: Proceedings of the first AFOSR international conference on DNS/LES. Columbus, OH, USA: Greyden Press; 1997. p. 137–47.
31. Nelson B, Lin TY, Quéméner Y, Lee YJ, Huang HH, Chien CY. Extreme typhoon loads effect on the structural response of an offshore wind turbine. In: Proceedings of the 7th PAAMES and AMEC 2016; 2016 Oct 13–14; Hong Kong, China [cited 2026 Aug 20]. Available from: https://www.crclass.org/en/2016%E6%8A%80%E8%A1%93%E5%8F%8A%E5%AD%B8%E8%A1%93%E8%AB%96%E6%96%87/.
32. He JY, Li QS, Chan PW. Reduced gust factor for extreme tropical cyclone winds over ocean. J Wind Eng Ind Aerodyn. 2021;208:104445. doi:10.1016/j.jweia.2020.104445.
33. Li L, Kareem A, Xiao Y, Song L, Zhou C. A comparative study of field measurements of the turbulence characteristics of typhoon and hurricane winds. J Wind Eng Ind Aerodyn. 2015;140:49–66. doi:10.1016/j.jweia.2014.12.008.
34. Sharma A, Brazell MJ, Vijayakumar G, Ananthan S, Cheung L, deVelder N, et al. ExaWind: open-source CFD for hybrid-RANS/LES geometry-resolved wind turbine simulations in atmospheric flows. Wind Energy. 2024;27(3):225–57. doi:10.1002/we.2886.
35. Gaertner E, Rinker J, Sethuraman L, Zahle F, Anderson B, Barter G, et al. Definition of the IEA 15-Megawatt offshore reference wind turbine. Golden, CO, USA: National Renewable Energy Laboratory; 2020. NREL/TP-5000-75698. [cited 2026 Aug 20]. Available from: https://www.nrel.gov/docs/fy20osti/75698.pdf.